sustainability

MDPI

Article

A Field-Calibrated UAV LiDAR Workflow-Level Case Study for Individual-Tree Inventory in Jilin Larch Plantations Using PCS, MCRG, and RHCSA

Chunyu Du [1,*], Xiongwei Liang [1,2,*], Ziqi Qiu [3], Shaopeng Yu [1], Yingning Wang [1,2], Nan Liu [1], Siyao Li [1] and Yufei Li [1]

[1] Cold Region Wetland Ecology and Environment Research Key Laboratory of Heilongjiang Province, Harbin University, Harbin 150086, China; shaopengyu1972@163.com (S.Y.); 14b927013@hit.edu.cn (Y.W.); ln09022026@163.com (N.L.); lsy128151@163.com (S.L.); lyf20051020@126.com (Y.L.)
[2] State Key Laboratory of Urban Water Resource and Environment, Harbin Institute of Technology, Harbin 150086, China
[3] College of Urban and Environmental Sciences, Central China Normal University, Wuhan 430079, China; qzqi666@126.com
* Correspondence: duchunyu402@163.com (C.D.); liangxiongwei007@163.com (X.L.)

Abstract

Sustainable forest management requires inventory workflows that provide spatially explicit structural information while retaining field-based calibration and uncertainty control. This case study evaluated a field-calibrated UAV LiDAR workflow for individual-tree inventory in middle-aged and near-mature larch plantations in Chuanying District, Jilin City, China. UAV laser scanning point-clouds were integrated with six 30 m × 30 m field plots to assess three individual-tree extraction algorithms: point-cloud segmentation (PCS), marker-controlled region growing (MCRG), and region-based hierarchical cross-section analysis (RHCSA). Algorithm performance was evaluated using plot-level recall, precision, F-score, localization RMSE, tree-height and crown-width accuracy, bootstrap confidence intervals, exploratory Wilcoxon signed-rank comparisons, and leave-one-plot-out stability checks. MCRG provided the most balanced numerical performance under the tested configuration, with a mean F-score of 0.845, compared with 0.808 for PCS and 0.827 for RHCSA. However, the MCRG-RHCSA paired difference was not robust across the six plots, and the analysis should be interpreted as a dataset-specific workflow comparison rather than a universal algorithm ranking. Tree height was estimated with comparatively high accuracy, whereas crown-width estimation remained weak, indicating that vertical canopy structure was more reliable than lateral crown delineation. After calibration assessment, the workflow was applied to 157.47 ha of UAV LiDAR survey areas and generated 219,996 algorithm-based detections. These outputs are best interpreted as a spatial decision-support layer for compartment updating, density screening, and field-inspection prioritization, not as an independently verified wall-to-wall stem census.

Keywords: UAV LiDAR; field-calibrated workflow; individual-tree inventory; larch plantation; case study; algorithm-based detections; uncertainty-aware workflow comparison; sustainable forest management

Academic Editors: Hongjun Li and Xiayuan Huang

Received: 14 June 2026
Revised: 7 July 2026
Accepted: 15 July 2026
Published: 17 July 2026

1. Introduction

Forest inventories increasingly need to support management decisions that are spatially explicit, repeatable, and auditable. Conventional field inventory remains indispensable for species identification, DBH measurement, destructive or semi-destructive calibration, and the interpretation of stand history. Its limitation is not scientific irrelevance but operational scalability: exhaustive tree-by-tree measurement becomes expensive when managers require repeated updates over large plantation areas, heterogeneous compartments, or short planning cycles [1–4]. This tension is central to sustainable forest management, where decisions about thinning, harvesting, pest surveillance, restoration, and carbon reporting depend on both accuracy and timeliness.

LiDAR remote sensing has altered the technical basis of forest inventory by measuring three-dimensional canopy and terrain structure rather than only two-dimensional spectral reflectance [2,3]. Individual-tree crown detection has been attempted with CHM-based local maxima, point-cloud clustering, region growing, watershed-style delineation, and increasingly data-driven or machine-learning workflows [5–24]. Comparable studies conducted in open-canopy conifer forests, ground-based LiDAR point clouds, coniferous plantations, and tropical forests further demonstrate that individual-tree delineation performance is strongly dependent on forest structure, sensor configuration, and segmentation strategy [25–29]. These approaches differ not only in accuracy but also in interpretability, parameter dependence, training-data requirements, and transferability across stand structures. For operational plantation inventories, an interpretable workflow may remain useful even when more complex algorithms exist, provided that its uncertainty and decision boundaries are explicit.

The critical scientific question is therefore not whether UAV LiDAR can produce visually plausible tree maps. The stronger question is whether a specific UAV LiDAR processing workflow produces tree-level information with known uncertainty and a defensible link to forest-management decisions. This distinction matters because a remote-sensing workflow can be efficient yet still unsuitable for high-stakes variables such as DBH, volume, biomass, or carbon stock if its errors are not calibrated with ground data [30]. Prior work on individual-tree inventory, crown-detection factors, tree matching, competition indices, crown-width estimation, and tree-height accuracy shows that these error sources are not interchangeable [31–38].

For sustainable forest management, the main value of UAV LiDAR does not lie only in dense point clouds or visually plausible tree maps. Its operational value depends on whether remotely sensed candidate tree objects can be linked to field-measured attributes, evaluated with transparent uncertainty, and interpreted within explicit decision boundaries. UAV LiDAR inventory should therefore be framed as a field-calibrated data-integration problem. LiDAR provides spatially continuous three-dimensional canopy structure, whereas field plots provide reference stems, DBH, crown measurements, species confirmation, and error control. This integration perspective is consistent with studies on LiDAR height and biomass estimation [39,40], individual-tree segmentation and delineation across sensor configurations [41–43], UAV and terrestrial laser scanning integration, pulse-density effects, and operational monitoring [44–48], and remote sensing for sustainable forest management [49,50]. Integrating these sources is necessary for converting algorithmic detections into defensible forest-management evidence.

The central challenge is therefore how to integrate LiDAR-derived structural objects with field-based reference information so that algorithmic outputs can be interpreted as management evidence. This study addresses three explicit research questions. First, within a field-plot calibration framework, which of PCS, MCRG, and RHCSA provides the most stable individual-tree detection? Second, which UAV LiDAR-derived tree attributes can be used reliably for management interpretation, and which should remain exploratory? Third, how can the workflow function as a spatial layer in a hybrid inventory system for compartment updating, density screening, and field-inspection prioritization?

The study is deliberately framed as a case study with explicit scope boundaries. It does not claim to identify a universal best individual-tree extraction algorithm. It evaluates three interpretable approaches within managed, structurally similar larch plantations in Jilin, China: point-cloud segmentation (PCS), marker-controlled region growing (MCRG), and region-based hierarchical cross-section analysis (RHCSA). This scope is appropriate because algorithm rankings are conditional on forest structure, acquisition density, parameter tuning, and reference-matching rules.

Larch plantations are operationally important and methodologically non-trivial. Their relatively regular spacing and coniferous crown architecture can make dominant and co-dominant trees detectable, but high density, crown overlap, suppressed trees, thinning history, and local site variation still create omission and boundary errors. Treating plantations as easy remote-sensing targets would therefore be a conceptual mistake. A useful workflow must demonstrate not only visually coherent segmentation but also quantified omission, commission, localization, and attribute errors.

The contribution of this study is threefold. First, it evaluates individual-tree extraction as a field-calibrated UAV LiDAR workflow rather than as a purely algorithmic segmentation exercise. Second, it compares three interpretable extraction algorithms using plot-level accuracy metrics and bootstrap uncertainty estimates, thereby avoiding overconfident conclusions from small numerical differences. Third, it proposes an evidence hierarchy for interpreting field-calibrated UAV LiDAR outputs in plantation management, distinguishing variables strongly supported by UAV LiDAR, such as tree height and spatial structure, from variables that require additional ground calibration, such as DBH, biomass, and carbon stock.

2. Materials and Methods

2.1. Study Area and Field Plots

Detailed field records of thinning history were not available. To partially address the missing stand-structure covariates, CHM rasters and retained tree-coordinate outputs were used to derive descriptive plot-level covariates. The CHM-based canopy-cover proxy, defined as the proportion of 0.25 m pixels higher than 2 m, ranged from 97.06% to 99.61%. Algorithm-derived nearest-neighbor spacing ranged from 2.53 m to 2.66 m for MCRG and from 2.77 m to 3.05 m for PCS. These variables are descriptive covariates only; they are not treated as causal explanations of algorithm performance. The spatial distribution of the three UAV survey areas and the six field plots is shown in Figure 1.

Six 30 m $\times$ 30 m larch plantation plots were selected from two UAV LiDAR survey areas using a stratified field design within accessible, structurally comparable compartments. The plots covered middle-aged and near-mature managed larch stands under moderate canopy closure and gentle to moderate terrain conditions. They represented the dominant plantation conditions available in the project area, but they do not represent young stands, overmature stands, heavily thinned stands, mixed forests, or steep terrain. Descriptive statistics for the six larch plantation field plots are summarized in Table 1.

Table 1. Descriptive statistics of the six larch plantation field plots.

Plot	Trees (n)	Mean Height (m)	Mean DBH (cm)	Mean Crown Width (m)	Age Class
1	128	15.58	14.71	2.26	Middle-aged
2	112	16.63	15.81	2.28	Middle-aged
3	122	16.75	16.15	3.06	Middle-aged
4	105	17.42	16.13	3.20	Middle-aged
5	101	17.18	16.38	3.02	Near-mature
6	107	17.00	15.61	2.30	Near-mature

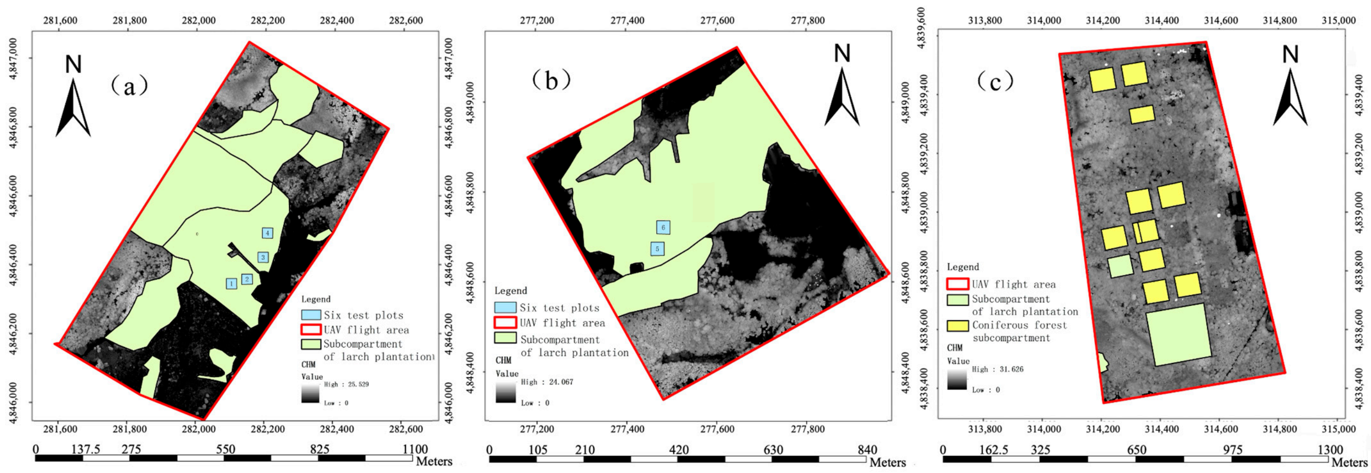

Figure 1. Locations of the UAV survey areas and sample plots. Panels (**a**–**c**) show survey areas 1–3, respectively. Legend elements are numbered and defined as follows: (1) blue rectangles, six 30 m × 30 m test plots; (2) red outline, UAV flight area; (3) light-green polygons, larch plantation sub-compartments; (4) yellow polygons in panel (**c**), coniferous forest sub-compartments; (5) grayscale background, CHM value, with lighter tones indicating greater canopy height; and (6) labels 1–6, identifiers of the six field plots.

This sampling design improves internal comparability among algorithms but limits external inference. Accordingly, all conclusions are expressed as case-study findings for structurally similar larch plantations rather than as regional performance estimates for Northeastern China.

The absence of elevation, slope, canopy closure, spacing, and thinning-history covariates also affects causal interpretation. If one algorithm performs better in a plot, the present dataset cannot determine whether the difference is driven by crown overlap, terrain-induced normalization error, local stocking, age-related crown form, or parameter suitability. The study can rank algorithms descriptively within the observed plots, but it cannot yet explain performance variation mechanistically. This limitation is explicitly carried into the discussion rather than being hidden behind pooled means.

2.2. UAV LiDAR Acquisition and Field-Reference Integration

UAV LiDAR data were acquired on 27 May 2022 using a Feima D200S UAV platform equipped with a RIEGL miniVUX-1UAV D-LiDAR200 sensor. The campaign used a terrain-following flight at 80 m, a flight speed of 6 m s^{-1}, 70% forward and side overlap, a 360° field of view, a pulse repetition frequency of 100 kHz, and a scan-frequency range of 10–100 Hz. The survey was conducted during the growing season under no-rain and low-wind conditions (approximately 1–3 m s^{-1}). The point clouds were registered to WGS 84/UTM Zone 52N, and the retained project record reports a mean point density of approximately 10 points m^{-2}.

To make the workflow auditable, Table 2 has been revised to report the retained flight, preprocessing, CHM, algorithm-parameter, and matching-rule metadata. Where the original raw processing logs or original matching logs were unavailable, the revised manuscript distinguishes retained parameters, reconstructed accuracy counts, and unresolved reproducibility limitations.

The field inventory recorded individual-tree position, species, four-direction crown width, DBH, tree height, and live-crown attributes. The evaluation was implemented within a field-supported reference framework, in which field measurements provided the basis for matching, calibration, and uncertainty interpretation. Tree height and crown/treetop reference interpretation were supported by UAV LiDAR point-cloud visualization and

CHM interpretation in some cases. This reference framework is appropriate for operational consistency assessment, although it is not equivalent to a fully independent validation design. Point-cloud previews for the six field plots are shown in Figure 2.

Table 2. Updated workflow metadata and retained parameter settings used for interpretation and reproducibility assessment.

Checklist Item	Available Information	Use in This Study
UAV platform and sensor	Feima D200S UAV platform (Shenzhen Feima Robotics Co., Ltd., Shenzhen, China) with RIEGL miniVUX-1UAV D-LiDAR200 sensor (RIEGL Laser Measurement Systems GmbH, Horn, Austria); point clouds registered to WGS 84/UTM Zone 52N.	Defines platform, sensor, and coordinate system for workflow-level reproducibility.
Survey campaign	27 May 2022 growing-season survey; terrain-following flight at 80 m, 6 m s^{-1}, 70% forward and side overlap, 360 degrees FOV, pulse repetition frequency 100 kHz, scan frequency 10–100 Hz, no rain and low wind.	Supports acquisition-level interpretation; not used to claim cross-campaign invariance.
Point density	Mean point density approximately 10 points m^{-2}; plot-level CHM-based canopy-cover proxy and algorithm-derived spacing are reported descriptively.	Supports survey-scale data-density reporting and descriptive stand-structure context.
Positioning and registration	Dual-frequency GNSS using GPS L1/L2, BeiDou B1/B2, and GLONASS L1/L2; 20 Hz sampling; reported positioning accuracy 5 cm; PPK/RTK and integrated operation mode; IMU roll/pitch/yaw accuracies ±0.010 degrees, ±0.010 degrees, and ±0.050 degrees.	Supports spatial matching at the workflow level; independent registration-error modeling was not performed.
Processing software	LiDAR360 V5.0 (GreenValley International Inc., Berkeley, CA, USA) and ArcGIS Desktop 10.8.2 (Esri, Redlands, CA, USA) were used for point-cloud processing, CHM interpretation, and reference editing.	Identifies the processing environment for workflow-level reproducibility.
Preprocessing and CHM	LiDAR360 v5.0 statistical outlier filtering, progressive TIN ground classification, normalization, DEM/DSM/CHM generation at 0.25 m, maximum-height CHM interpolation, pit filling to 0.5 m, and 3 × 3 median filtering.	Provides retained CHM and preprocessing settings; full CHM-resolution sensitivity analysis was not reconstructed.
Algorithm implementation	PCS: 2 m minimum height, 4 m maximum crown radius, 0.6 m clustering distance, minimum 30 points, highest normalized point as the seed. MCRG: 5 × 5 local-maximum window selected from 3 × 3/5 × 5/7 × 7 comparison, 2 m seed threshold, <0.3 m height-difference rule, 4 m maximum radius, 1.2 m^2 minimum crown area. RHCSA: 2 m threshold, 0.1 m vertical slice interval, marker-watershed splitting, roundness 0.85, 500-pixel pseudo-crown threshold, 1.0 m^2 minimum area, 4 m maximum crown width.	Documents retained operational settings; ranking remains a case-study workflow comparison, not a universal algorithm benchmark.
Field-reference data	Field inventory recorded tree position, species, DBH, height, crown width, and live-crown attributes.	Provides the reference basis for matching, calibration, and attribute assessment.
Matching and accuracy outputs	One-to-one nearest-neighbor matching between detected crown center and RTK stem XY coordinate; 2 m horizontal threshold; nearest detection retained under conflicts; unmatched detections classified as FP and unmatched reference trees as FN; outside-plot crown centers excluded.	Defines TP/FP/FN logic. Reconstructed counts are labeled as reconstructed rather than original matching logs.

Note: Parameters listed in this table were recovered from the supplied Supplementary Materials and retained project records. Items still lacking raw processing logs, complete balanced parameter-optimization records, or original matching audit logs are treated as reproducibility limitations.

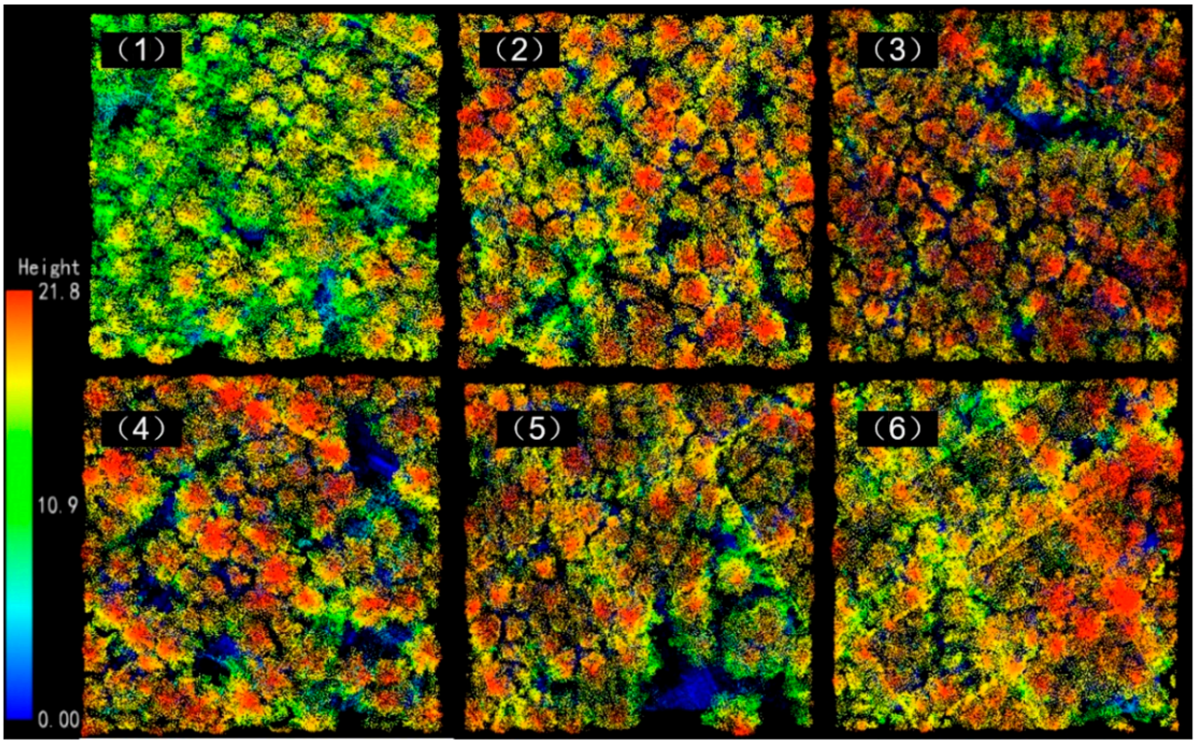

Figure 2. UAV LiDAR point-cloud previews of the six field plots. Panel (**1**) shows field plot 1; panel (**2**) shows field plot 2; panel (**3**) shows field plot 3; panel (**4**) shows field plot 4; panel (**5**) shows field plot 5; and panel (**6**) shows field plot 6. The color gradient represents normalized canopy height (m).

The six plots provide a useful internal comparison of algorithms under similar plantation conditions, but they do not form a probabilistic regional sample of all larch plantations in Northeastern China. The study therefore supports comparative and operational claims within the sampled domain. Regional claims would require stratified sampling across age classes, stocking levels, slope classes, thinning histories, and canopy closures.

Incomplete acquisition records have practical consequences for repeat monitoring. If a future acquisition uses a different altitude, scan angle, overlap, season, or strip-adjustment procedure, changes in detected tree count may reflect acquisition geometry rather than real growth, mortality, or thinning. For sustainability monitoring, such confounding is not a minor reporting issue; it directly affects trend interpretation. The workflow should therefore be accompanied by a minimum metadata record for every survey campaign.

Within this field-supported reference framework, field measurements, stem maps, orthophotos, and point-cloud visualization provided complementary evidence. The field plots were not used merely as external validation points. They provided the reference structure through which LiDAR-derived candidate tree objects were interpreted, matched, and evaluated.

2.3. Point-Cloud Preprocessing and CHM Generation

The preprocessing workflow included noise removal, ground classification, normalization, and CHM production. Low and high outliers were removed to reduce spurious points caused by ranging error, multi-path effects, or non-vegetation targets. Ground and non-ground points were separated using a progressive triangulated irregular network filtering approach, a family of methods widely used in forested terrain because it incrementally densifies a terrain surface while evaluating candidate ground points against slope and distance criteria [51–57].

Point-cloud normalization was performed by subtracting local ground elevation from each point elevation. Noise removal used LiDAR360 v5.0 statistical outlier filtering with a five-standard-deviation threshold for high and low outliers. Ground points were classified using progressive TIN densification. DEM, DSM, and CHM rasters were generated at 0.25 m resolution; CHM generation used maximum-height interpolation, LiDAR360 pit filling with a maximum filling depth of 0.5 m, and 3 × 3 median filtering before segmentation.

A reproducible inventory workflow must distinguish direct and derived variables. Algorithm-based detections, treetop positions, and CHM-based heights are direct outputs of the UAV LiDAR processing chain. Crown width is a derived output dependent on segmentation boundaries and crown-shape assumptions. DBH, volume, biomass, and carbon variables would require additional allometric models and ground calibration; they are not directly measured by the present UAV LiDAR workflow.

Ground filtering is particularly important in this landscape because even small DEM errors translate directly into normalized height errors. A tree that is measured as too tall or too short may shift local maxima, alter the height threshold at which a crown enters the segmentation process, and change whether a candidate object satisfies minimum-height rules. The error, therefore, propagates from terrain processing into detection, localization, and attribute estimation rather than remaining a separate preprocessing issue.

CHM settings mediate a fundamental trade-off. The retained 0.25 m CHM preserves local crown structure but may increase noise and produce multiple maxima within a single crown. The 3 × 3 median filter reduces local noise but can merge adjacent crowns and suppress small trees. A full CHM-resolution sensitivity experiment could not be reconstructed without the original point-cloud processing chain, but the revised workflow reports the retained CHM settings and treats this as a reproducibility boundary.

2.4. Individual-Tree Extraction Algorithms

PCS assigns point-cloud observations to tree clusters according to vertical ordering and distance relationships. The retained PCS configuration used a 2 m minimum tree-height threshold, a 4 m maximum crown radius, a 0.6 m clustering-distance threshold, a minimum of 30 laser points per cluster, and the normalized global-height maximum as the treetop seed rule. These settings are reported as the operational LiDAR360 configuration used in this case study rather than as an optimized universal parameter set.

MCRG detects local maxima in the CHM and uses them as crown markers. The retained workflow compared 3 × 3, 5 × 5, and 7 × 7 local-maximum windows and used the 5 × 5 window because it gave the best retained F-score in the project record. The MCRG configuration used a 2 m seed-height threshold, a height-difference rule of <0.3 m for adding adjacent pixels to a crown region, a 4 m maximum crown radius, and a 1.2 m^2 minimum crown area. It remains vulnerable to suppressed trees that do not generate independent local maxima and to merged crowns where the growth rule crosses real tree boundaries.

RHCSA treats the CHM as a vertically layered surface. Horizontal slices were evaluated from the canopy top downward, with a 2 m minimum canopy-height threshold and a 0.1 m vertical slice interval. The retained implementation used marker-watershed splitting for merged regions, a roundness threshold of 0.85, a 500-pixel area threshold for removing pseudo-crowns, a 1.0 m^2 minimum region area, a 4 m maximum crown-width limit, and termination at the 2 m minimum-height threshold when no new crown sections emerged. The complete field-calibrated workflow is summarized in Figure 3.

For all algorithms, the comparison should be interpreted as an applied workflow comparison rather than a fully optimized algorithm benchmark. Without a complete parameter-sensitivity experiment, a higher F-score may reflect a better fit between the chosen settings and the sampled stand structure rather than an intrinsic advantage of the algorithm class.

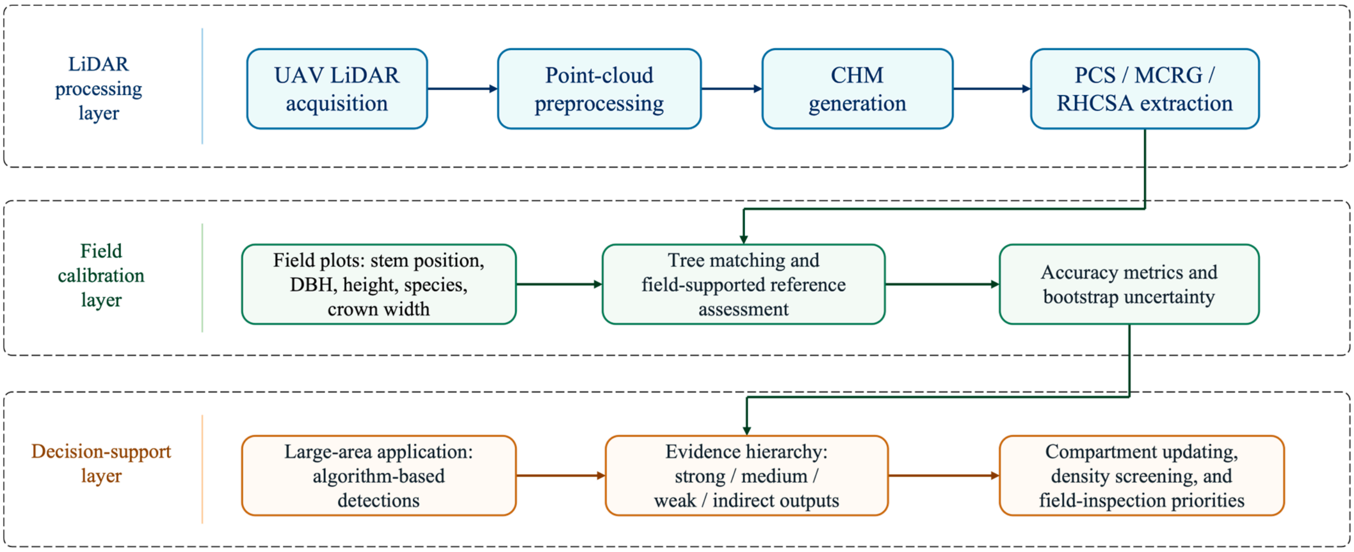

Figure 3. Field-calibrated UAV LiDAR workflow linking point-cloud processing, field-reference assessment, uncertainty evaluation, large-area application, and management evidence classification.

Algorithm-based detections were matched to reference trees using a one-to-one nearest-neighbor rule. A detected crown was classified as a true positive when its crown center was within a 2 m horizontal distance of the RTK-measured stem XY coordinate. When multiple detected crowns matched the same field tree, only the nearest detection was retained as the true positive and the remaining detections were classified as false positives. Detected crowns without a reference tree within 2 m were classified as false positives, and field trees without a detected crown within 2 m were classified as false negatives. Crowns whose centers fell outside the 30 m $\times$ 30 m plot boundary were excluded from plot-level accuracy statistics.

The three algorithms also differ in interpretability. PCS is transparent because its errors can often be traced to point-distance thresholds and cluster rules. MCRG is interpretable because local maxima and growth constraints can be inspected on the CHM. RHCSA is conceptually rich because it uses the vertical emergence of crown regions, but its implementation can become more difficult to audit if merged-region handling is not fully documented. For management adoption, interpretability is not secondary to accuracy; it determines whether forest officers can diagnose failures and trust repeated outputs.

A fair comparison requires comparable tuning effort. The revised manuscript therefore reports the retained parameter settings and avoids presenting the ranking as an intrinsic algorithm property. The study evaluates the practical configuration available in the project workflow, with the explicit caveat that a balanced optimization protocol across PCS, MCRG, and RHCSA would be required for a stronger algorithm-benchmark claim.

2.5. Accuracy Assessment and Operational Throughput Metrics

The archived accuracy results included plot-level recall, precision, F-score, localization RMSE, and tree-attribute accuracy metrics derived from true-positive (TP), false-positive (FP), and false-negative (FN) counts. Supplementary Table S2 reports the reconstructed plot-level TP/FP/FN count table, with reconstructed values clearly marked where they were derived from retained recall, precision, and reference-count records rather than from original matching logs. These metrics separate omission, commission, and spatial displacement, which have different management implications [31–38].

Tree-attribute accuracy was assessed using R^2 and RMSE for tree height and crown width. Height is expected to be more reliable because the vertical canopy surface is directly observed in the normalized point cloud and CHM. Crown width is expected to be less reliable because it depends on lateral boundary delineation, crown overlap, CHM smoothing, and geometric assumptions about crown shape.

Operational coverage throughput was evaluated by comparing the field tally survey with the UAV LiDAR campaign. The field survey covered six 30 m $\times$ 30 m plots, totaling 0.54 ha and 675 trees, over approximately four field days. UAV LiDAR data were acquired over 157.47 ha in one field day and generated 219,996 algorithm-based detections after processing. This wording separates acquisition coverage from post-processing output and avoids describing detections as independently verified trees.

The throughput comparison is not a cost–benefit analysis. Processing time, software licensing, equipment cost, operator expertise, manual quality control, flight planning, and uncertainty correction were not included. Therefore, throughput ratios are reported as operational coverage indicators, not as accuracy-adjusted productivity or economic efficiency.

For structurally similar stands with local field plots, an omission-adjusted stem count can be calculated as $N_{adj} = N_{det}/\text{recall}$. Using the mean MCRG recall of 0.745, the total of 219,996 detections would correspond to an illustrative omission-adjusted count of approximately 295,300 trees. This value is not reported as a final inventory estimate because the recall estimate comes from only six plots and may not transfer to all surveyed compartments.

Omission and commission errors have different consequences. Omission of suppressed trees may lead to underestimation of stem density and overstatement of mean tree size if missed stems are smaller than detected stems. Commission errors can inflate stem density and create false spatial hotspots. Localization error matters when outputs are used for repeated monitoring, thinning navigation, or matching across time. The metric set, therefore, needs to be interpreted in relation to management use rather than as a single accuracy score.

The throughput comparison is intentionally conservative in its interpretation. A one-day UAV LiDAR acquisition window is meaningful for operational planning, but it is not equivalent to a one-day finished inventory product. Data transfer, trajectory processing, classification, segmentation, quality control, map production, and reporting require additional labor and time. Those costs do not erase the spatial-coverage advantage, but they must be included before making economic claims about efficiency.

2.6. Statistical Treatment of Small-Sample Uncertainty

The sample size is small at the plot level (n = 6). Treating the mean F-score alone as decisive would overstate the evidence. This study, therefore, reports plot-level metrics, nonparametric bootstrap confidence intervals for mean F-score and paired F-score differences, exploratory Wilcoxon signed-rank comparisons, and a leave-one-plot-out stability check. All resampling and paired comparisons use the plot as the unit of inference.

Formal parametric tests are not emphasized because six plots provide limited information about the distribution of errors. Exploratory Wilcoxon signed-rank tests gave $p = 0.0625$ for MCRG versus PCS and $p = 0.6875$ for MCRG versus RHCSA. These tests support cautious interpretation: MCRG showed a consistent numerical advantage over PCS in the retained plot metrics but was not statistically separable from RHCSA.

The bootstrap analysis uses plots rather than individual trees as the resampling unit because trees within a plot are not statistically independent. They share stand structure, acquisition geometry, preprocessing history, and algorithm settings. Treating hundreds of trees as independent replicates would artificially narrow confidence intervals and overstate evidence. Plot-level resampling is less powerful, but it better reflects the actual design.

The resulting confidence intervals should be read as descriptive uncertainty, not as definitive population inference. With six plots, the bootstrap distribution is constrained by the observed plot set and cannot represent unobserved stand structures. Its value is mainly disciplinary: it prevents the manuscript from presenting small numerical differences as decisive and forces the conclusion to match the strength of the design.

3. Results

3.1. Stand Structure and Data Characteristics

The six field plots showed broadly similar tree-height and DBH distributions, as expected in managed larch plantations. Mean height varied within a relatively narrow range of 1.84 m across plots, and mean DBH varied by 1.67 cm. Crown width showed somewhat greater variation, from 2.26 m to 3.20 m. This structure supports an internally coherent algorithm comparison but does not represent the full structural range of plantation or mixed forests.

The UAV LiDAR point clouds captured dense canopy surfaces and visible crown-level variation. Dominant and co-dominant larch crowns were often separable, but crown overlap remained substantial in several plot areas. This pattern anticipates the quantitative results: precision was high, indicating that many detected crowns corresponded to reference trees, whereas recall was lower, indicating omission of trees without distinct canopy expression.

The narrow range of DBH and height also means that the study provides a relatively favorable test of height estimation but a limited test of model extrapolation. Algorithms may perform differently in younger plantations with smaller crowns, older stands with stronger crown asymmetry, or recently thinned compartments with irregular gaps. The results should therefore be viewed as evidence for a coherent plantation subset rather than as a complete evaluation across the larch rotation.

3.2. Individual-Tree Segmentation Performance

Plot-level segmentation results are reported in Table 3. MCRG produced the highest mean F-score (0.845), followed by RHCSA (0.827) and PCS (0.808). Mean recall was 0.745 for MCRG, 0.727 for RHCSA, and 0.690 for PCS. Mean precision was high for all algorithms: 0.968 for MCRG, 0.970 for PCS, and 0.947 for RHCSA. Thus, the principal limitation was omission rather than commission. Representative segmentation outputs for the three algorithms are shown in Figure 4.

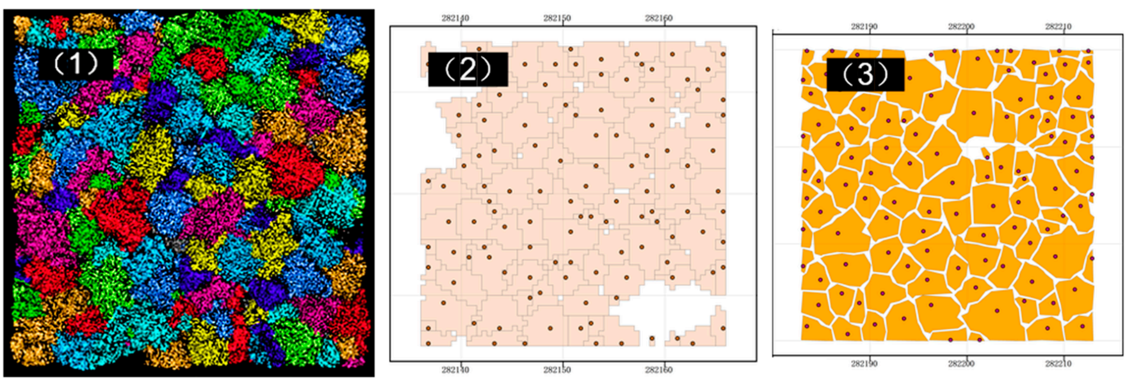

Figure 4. Representative segmentation outputs selected for the three individual-tree extraction algorithms: (**1**) PCS output for field plot 1; (**2**) MCRG output for field plot 2; and (**3**) RHCSA output for field plot 3. Colors distinguish adjacent algorithm-derived tree segments and are not ordinal values; small dark/red dots in panels (**2**,**3**) denote tree-center points. Because the panels represent different field plots, formal quantitative comparisons among algorithms are reported in Tables 3 and 4.

https://doi.org/10.3390/su18147321

Table 3. Plot-level individual-tree segmentation accuracy of the three algorithms.

Algorithm	Plot	Recall	Precision	F-Score	Localization RMSE (m)
PCS	1	0.64	0.95	0.80	0.73
PCS	2	0.67	1.00	0.80	0.79
PCS	3	0.62	1.00	0.76	0.84
PCS	4	0.69	0.88	0.77	0.80
PCS	5	0.82	1.00	0.90	0.81
PCS	6	0.70	0.99	0.82	0.88
MCRG	1	0.65	0.95	0.80	0.74
MCRG	2	0.74	1.00	0.85	0.89
MCRG	3	0.72	0.99	0.83	0.96
MCRG	4	0.72	0.88	0.79	0.75
MCRG	5	0.84	1.00	0.91	0.83
MCRG	6	0.80	0.99	0.89	0.92
RHCSA	1	0.64	0.98	0.81	0.78
RHCSA	2	0.82	0.99	0.90	0.81
RHCSA	3	0.67	0.85	0.75	0.71
RHCSA	4	0.56	0.86	0.68	0.78
RHCSA	5	0.91	1.00	0.95	0.94
RHCSA	6	0.76	1.00	0.87	1.04

Table 4. Bootstrap uncertainty for mean and paired F-score estimates across six plots.

Algorithm/Contrast	Metric	Mean or Paired Difference	Bootstrap 95% CI	Interpretation
PCS	F-score	0.808	0.777–0.848	Lower mean balance; high precision but lower recall.
MCRG	F-score	0.845	0.810–0.880	Highest numerical mean under the tested configuration.
RHCSA	F-score	0.827	0.755–0.897	Wider uncertainty across plots; strong in some plots but unstable.
MCRG-PCS	Paired F-score difference	0.037	0.015–0.058	Numerical advantage over PCS in all six plots.
MCRG-RHCSA	Paired F-score difference	0.018	−0.027–0.068	Difference not robust with six plots; interpret cautiously.

Bootstrap resampling used plots as the sampling unit. CIs are descriptive because n = 6.

The plot-level pattern matters. RHCSA achieved the highest F-score in plot 5 and strong performance in plot 2, but it also performed poorly in plot 4. MCRG was more even across plots and showed numerical advantages over PCS in F-score across all six plots. Localization RMSE differed little among algorithms, indicating that the main algorithmic difference was whether a tree was detected rather than where matched trees were positioned.

The leave-one-plot-out stability check gave the same general interpretation. After omitting one plot at a time, MCRG remained numerically highest in five of six omissions and tied with RHCSA when Plot 4 was omitted. This supports MCRG as the most stable default option in this case study, while confirming that the MCRG-RHCSA separation is not robust enough for a universal ranking.

Bootstrap uncertainty estimates and paired comparisons temper the algorithm ranking (Table 4). MCRG had the highest mean F-score and a positive paired difference relative to PCS, but the Wilcoxon signed-rank test was exploratory and borderline (p = 0.0625). The paired F-score difference between MCRG and RHCSA had a bootstrap 95% CI that crossed zero, and the Wilcoxon test was not significant ($p = 0.6875$). The defensible conclusion is therefore not that MCRG is universally superior, but that it showed the most balanced numerical performance under this dataset and processing configuration.

Supplementary Table S2 reports plot-level TP, FP, and FN counts, with reconstructed values clearly marked as reconstructed rather than original raw matching logs. The reference-tree denominator in Table S2 represents the subset of field stems with usable georeferenced crown/stem matching records retained in the revision materials, rather than the full plot stem tally. Therefore, it is smaller than the total number of field-measured stems reported in Table 1. Accordingly, recall, precision, F-score, and localization RMSE are interpreted as workflow-level accuracy metrics rather than as a complete re-estimation of the full plot census.

The high precision values indicate that the algorithms rarely produced large numbers of unsupported detections in the tested plots. From a management perspective, this makes the maps useful for locating dominant-tree structure and planning field checks. The lower recall values are more problematic for estimating density or mortality because missed trees are invisible in the output unless corrected with plot data. This asymmetry explains why the workflow is more defensible for structural mapping than for uncorrected stem census.

The plot-specific behavior also suggests that algorithm choice should be conditional rather than fixed. A workflow could use MCRG as the default method, then flag compartments where local crown overlap, unusual crown form, or low point density make RHCSA or alternative settings worth testing. Such adaptive processing would be more robust than selecting one algorithm globally based on a small mean advantage.

3.3. Tree-Attribute Estimation Accuracy

Tree height was estimated with comparatively high accuracy (Table 5). PCS achieved a mean-height $R^2 = 0.81$ and RMSE = 0.82 m; MCRG achieved a mean $R^2 = 0.80$ and RMSE = 0.81 m; RHCSA achieved a mean $R^2 = 0.74$ and RMSE = 0.83 m. Differences among algorithms were small relative to the absolute height error, suggesting that normalized canopy height was captured consistently across the tested methods.

Table 5. Mean tree-attribute estimation accuracy.

Algorithm	Height R^2	Height RMSE (m)	Crown Width R^2	Crown Width RMSE (m)
PCS	0.81	0.82	0.35	1.14
MCRG	0.80	0.81	0.35	0.99
RHCSA	0.74	0.83	0.13	0.94

Crown-width estimation was substantially weaker. PCS and MCRG both produced mean crown-width $R^2 = 0.35$, while RHCSA produced $R^2 = 0.13$. Crown-width RMSE ranged from 0.94 m to 1.14 m, but RMSE alone is not sufficient because low R^2 indicates poor explanation of individual variation. Because paired field-versus-algorithm crown-width residuals were not supplied, systematic over- or underestimation cannot be quantified beyond these aggregate metrics. Crown width should therefore be treated as a low-confidence individual-tree attribute in this workflow.

The height result is practically meaningful because stand height and dominant height are central to site-quality assessment, growth monitoring, and compartment updating. An RMSE near 0.8 m is likely acceptable for stand-level mean-height or dominant-height summaries in structurally similar plantations, especially when estimates are aggregated to stand or compartment scale. It is not sufficient for applications that require precise individual-tree growth increments over short intervals, such as less than three years, where small biological changes can be confounded with measurement error.

The crown-width result has a different implication. A moderate RMSE can appear acceptable when judged only in meters, but the low R^2 indicates a weak ability to explain individual variation. In other words, the workflow may produce crown-width values within a plausible numeric range while still failing to rank trees reliably by crown size. This distinction between plausible values and explanatory accuracy is important for avoiding overuse of crown-derived variables in downstream models.

3.4. Field-Calibrated Large-Area Application and Operational Coverage

The large-area application was interpreted through the field-plot accuracy assessment rather than as an uncalibrated wall-to-wall census. Therefore, the 219,996 mapped units are reported as algorithm-based detections whose management value depends on the recall, precision, and attribute reliability quantified in the six reference plots. They should not be interpreted as independently verified stems.

Within complete sub-compartments (Table 6), the workflow generated 21,274 algorithm-based detections across 24.80 ha in survey area 1 *, 13,202 detections across 15.21 ha in survey area 2 *, and 10,623 detections across 10.54 ha in survey area 3 *. Across all forest survey areas (Table 7), UAV LiDAR processing generated 219,996 algorithm-based detections over 157.47 ha. These detections were interpreted as calibrated remote-sensing units rather than verified field stems.

Table 6. Algorithm-based UAV LiDAR outputs for complete larch or conifer sub-compartments.

Survey Unit	Forest Type	Area (ha)	Sub-Comp. (n)	Algorithm-Based Detections (n)	Mean Height (m)	Mean Crown Width (m)
1 *	Larch plantation	24.80	10	21,274	14.73	3.38
2 *	Larch plantation	15.21	2	13,202	17.04	3.42
3 *	Coniferous forest	10.54	14	10,623	17.76	2.23

Asterisks indicate complete sub-compartments within UAV LiDAR survey areas.

Table 7. Algorithm-based UAV LiDAR outputs for all surveyed forest areas.

Survey Unit	Area (ha)	Algorithm-Based Detections (n)	Mean Height (m)	Mean Crown Width (m)
1	53.76	69,042	12.79	2.47
2	33.73	37,435	15.39	2.67
3	69.98	113,519	18.40	2.57
Total	157.47	219,996	-	-

Operational coverage was large (Table 8). The UAV LiDAR campaign covered 291.61 times more area than the six field plots in total and 1166.44 times more area per day. It generated 325.92 times more counted units than the field tally and 1303.68 times more counted units per day. These ratios are not accuracy-adjusted productivity measures; they quantify acquisition and processing scale under the stated exclusions.

The large-area output is useful because individual detections can be aggregated by compartment, thinning block, slope position, or risk zone. Nevertheless, spatially explicit output does not eliminate error. If missed trees are concentrated below dominant crowns or in dense patches, uncorrected compartment totals may be biased. Large-area applications, therefore, require plot-based calibration and targeted field checks rather than blind acceptance of the algorithm map.

https://doi.org/10.3390/su18147321

Table 8. Operational coverage and counted-unit throughput of the field survey and UAV LiDAR survey.

Metric	UAV LiDAR Algorithm-Based Output	Field Tally Survey	Ratio
Time (days)	1	4	-
Area (ha)	157.47	0.54	291.61
Counted units (n)	219,996	675	325.92
Area per day (ha/day)	157.47	0.135	1166.44
Counted units per day	219,996.00	168.75	1303.68

Processing time, software licensing, equipment cost, operator expertise, manual quality control, flight planning, and uncertainty correction were not included.

The distinction between complete sub-compartments and all surveyed forest areas is not merely a formatting issue. Larch-specific algorithm performance was assessed in plantation plots, whereas all surveyed forest polygons may contain broader conifer or mixed structures. Combining them in one table would imply that the same evidence base supports all rows equally. Splitting the tables makes the evidentiary hierarchy explicit.

Large-area detections can support management even when absolute stem counts are uncertain. Relative density surfaces, height gradients, and spatial clusters of unusual structure can guide where field crews should inspect first. This is a defensible use because the map functions as a prioritization layer. In contrast, using the same output as a final stand register would require stronger omission correction and independent checks.

4. Discussion

4.1. Evidence for MCRG and the Limits of Algorithm Ranking

MCRG showed the most balanced numerical performance in the available dataset. This result is plausible because the algorithm combines local maximum detection with spatially coherent crown expansion, which suits relatively regular coniferous plantation crowns. The method can retain high precision while improving recall relative to purely point-distance segmentation [5,17,21–24].

The evidence does not justify an unconditional claim that MCRG is the best algorithm for larch plantations, let alone for other forests. The difference between MCRG and RHCSA was small and uncertain, with only six plots. A strong algorithmic claim would require independent test plots, balanced parameter optimization, CHM and matching-rule sensitivity analyses, and forest-structure covariates that explain when each method fails.

The practical conclusion is narrower but operationally useful: MCRG is recommended as the default candidate for this dataset and structurally similar larch plantations, but this recommendation is conditional on local calibration. A management workflow should retain field plots specifically to estimate omission error and to detect changes in algorithm performance across stand density, age class, and thinning history.

The most likely failure mode for MCRG remains under-detection in vertically suppressed or laterally merged crowns. This is not a minor residual error because suppressed trees can contribute substantially to stand density and competition, even if they contribute less to canopy height. A method optimized around visible canopy maxima will tend to represent the dominant canopy better than the full stem population [23,25,32,34].

This limitation also affects the interpretation of height distributions. If shorter or suppressed trees are preferentially missed, the detection-based height distribution may be biased upward. Mean height estimates for matched detections can still be accurate relative to matched reference trees, while the population-level height distribution remains biased because missing trees are not included. This is another reason why recall correction and field calibration are necessary.

4.2. Evidence Hierarchy for Sustainable Plantation Management

The main management contribution of this study is not the selection of a single segmentation algorithm, but the classification of UAV LiDAR-derived outputs into different evidence levels for sustainable plantation management. A workflow that acquires wall-to-wall structural information over hundreds of hectares can help managers update compartment records, identify spatial heterogeneity, plan field visits, and monitor growth [1–4,49,50]. These benefits are defensible only for variables whose error is compatible with the decision being made.

Table 9 provides the evidence hierarchy for interpreting field-calibrated UAV LiDAR outputs. Stand mean height and dominant height are the strongest outputs. Individual-tree spatial distribution is useful for density screening and thinning pre-assessment, but remains sensitive to the omission of suppressed trees. Crown width is weak at the individual-tree level. DBH, volume, biomass, and carbon accounting require separate ground calibration and uncertainty propagation.

Table 9. Evidence hierarchy of field-calibrated UAV LiDAR outputs for sustainable plantation management.

Output	Evidence Strength	Defensible Use	Boundary Condition
Stand mean height and dominant height	Strong	Compartment structural updating, growth monitoring, and prioritizing field visits.	Requires consistent acquisition and terrain normalization.
Individual-tree spatial distribution	Medium-strong	Density mapping, thinning screening, and locating variable-structure patches.	Missed suppressed trees can bias local density.
Stem density	Medium	Relative comparison among structurally similar compartments and bias-adjusted estimates with plot calibration.	Do not use as an uncorrected census.
Crown width	Weak	Exploratory structural descriptor only.	Not high-confidence at the individual-tree level.
DBH, volume, and biomass	Indirect	Possible only through local allometry and ground DBH calibration.	Not directly measured by UAV LiDAR in this workflow.
Carbon accounting	Insufficient as stand-alone evidence	Auxiliary structural layer for management strata and monitoring.	Requires independent biomass models and uncertainty propagation.

This hierarchy prevents a common overclaim in remote-sensing manuscripts: equating a fast structural map with a complete forest inventory. The present workflow extends the spatial reach of field inventory and is strongest as the spatial layer in a hybrid inventory system. Ground plots remain necessary for variables that cannot be directly inferred from canopy geometry.

A hybrid deployment would use UAV LiDAR to generate continuous structural maps, field plots to calibrate omission and allometry, and targeted checks in locations where the algorithm is most likely to fail. This design is more scientifically defensible than either a purely plot-based approach with poor spatial coverage or a purely remote-sensing approach with insufficient ground control.

For thinning, UAV LiDAR-derived tree maps can identify dense patches, access constraints, and candidate areas for field inspection, but they should not automatically determine which individual trees are removed. Silvicultural decisions depend on species, stem quality, health, spacing, regeneration goals, and operational constraints that are not fully captured by canopy geometry. The appropriate role of UAV LiDAR is therefore screening and spatial grouping rather than automated prescription.

For carbon accounting, the evidentiary bar is higher. Carbon estimates require biomass equations, DBH or diameter proxies, wood density, species composition, and uncertainty propagation [30,39,40]. The present workflow provides useful structural layers, especially height and spatial density, but it does not independently validate biomass. Treating algorithm-based detections as carbon units would be a misuse of the evidence unless integrated with ground plots and local allometry.

4.3. Why Crown Width Remains Weak

Crown-width estimation is the weakest attribute result because lateral crown boundaries are not directly observed with the same clarity as canopy height. In dense plantations, neighboring crowns interpenetrate, CHM smoothing can remove boundary detail, and a circular-crown assumption simplifies asymmetric crown form. These mechanisms explain why crown-width R^2 remained low even where RMSE values appeared moderate [35–38]. Because paired crown-width residuals were unavailable, we avoided inferring systematic bias direction and restricted the interpretation to aggregate explanatory power and absolute error.

Future work should evaluate whether full 3D point-cloud crown volumes, voxel features, alpha-shape crown envelopes, multi-view UAV imagery, or spectral fusion improve lateral boundary delineation [6–10,58–60]. Such methods should be tested within the target plantation structures rather than assumed to transfer from other forest types. Until then, crown width should be treated as exploratory rather than operationally decisive.

The weakness of crown width also limits derived variables that depend on crown area. Competition indices, crown closure estimates, and inferred growing-space metrics may inherit boundary errors even when height is accurate. Any management system using crown-based indicators should therefore evaluate whether decisions change materially when crown-width error is propagated through the calculation.

4.4. Limitations and Future Improvements

Five limitations define the evidentiary boundary of this study. First, the field-supported reference framework is appropriate for operational consistency assessment, but it is not equivalent to a fully independent validation design because treetop and crown-reference interpretation partly relied on UAV LiDAR visualization. The exact proportion of reference trees assisted by LiDAR visualization was not retained and should be recorded in future studies.

Second, several retained parameters have now been reported, including flight geometry, CHM resolution and smoothing, algorithm thresholds, and the 2 m matching rule. However, the original raw processing logs, a full balanced parameter-optimization history, and original matching audit logs were not fully available. This limits parameter-level reproducibility and rules out claims about algorithm optimization.

Third, six plots support an internally coherent comparison but cannot represent the full structural range of larch plantations, mixed forests, broadleaf stands, terrain classes, or thinning histories. Transferability should be tested with stratified plots across stand age, stem density, canopy closure, slope, and management history.

Fourth, the study did not conduct a full CHM-resolution or algorithm–parameter–sensitivity analysis. Future work should vary CHM resolution, smoothing, local-maximum windows, MCRG growth criteria, crown-radius constraints, and matching rules, and should report bias-corrected large-area estimates with uncertainty intervals. Fifth, future studies should retain paired crown-width residual data so that systematic crown-width bias can be distinguished from random scatter. Table 10 summarizes the main error sources and mitigation options.

Table 10. Main error sources, bias directions, and mitigation options.

Error Source	Likely Direction of Bias	Mitigation Strategy
Suppressed or co-dominant trees lacking visible canopy maxima	Under-detection; recall decreases.	Use plot-level omission correction and targeted field checks in dense patches.
CHM smoothing and pit filling	Can merge crowns or shift local maxima.	Report CHM grid, smoothing kernel, and sensitivity tests.
Ground filtering error in forest terrain	Height bias propagates to tree height and local maxima.	Report filtering parameters and independent terrain checks.
Field-supported reference interpretation using UAV LiDAR visualization	Potential optimistic agreement for crown and treetop locations.	Described as a field-supported reference assessment, not a fully independent validation.
Allometric DBH/biomass conversion	Model-dependent volume or biomass bias.	Use local DBH plots and propagate uncertainty.

5. Conclusions

This case study evaluated a field-calibrated UAV LiDAR workflow for individual-tree inventory in managed larch plantations in Jilin, China. MCRG provided the most balanced numerical performance under the tested configuration, with a mean F-score = 0.845, compared with 0.808 for PCS and 0.827 for RHCSA. Because the MCRG-RHCSA paired difference was uncertain with six plots, and because parameter sensitivity was not fully reconstructed, the result should be interpreted as a dataset-specific workflow finding rather than a universal algorithm ranking.

Tree height was estimated with relatively high accuracy, whereas crown-width estimation remained weak. Applied across 157.47 ha, the workflow generated 219,996 algorithm-based detections. The main contribution is the evidence hierarchy summarized in Table 9, which separates strong, medium, weak, and indirect UAV LiDAR outputs for management interpretation.

This evidence hierarchy supports the use of field-calibrated UAV LiDAR as a spatial decision-support layer within hybrid plantation inventory systems. The workflow can support compartment updating, density screening, and field-inspection prioritization in structurally similar larch plantations. Variables such as DBH, biomass, and carbon accounting require additional ground calibration and uncertainty propagation, and broader scientific generalization will require larger stratified datasets, independent validation plots, and balanced parameter optimization.

Supplementary Materials: The following supporting information can be downloaded at: https://www.mdpi.com/article/10.3390/su18147321/s1. The supplementary package includes Table S1, retained UAV LiDAR acquisition, preprocessing, CHM, algorithm-parameter, and matching metadata; Table S2, reconstructed plot-level TP/FP/FN counts and matching definitions; and Table S3, CHM-based canopy-cover proxy and algorithm-derived nearest-neighbor spacing. Data note: Table S2 is reconstructed from retained project records and supplied revision materials and should be interpreted as workflow-level documentation rather than original raw matching logs.

Author Contributions: Conceptualization, C.D. and X.L.; methodology, C.D., X.L. and Z.Q.; software, Z.Q., S.Y. and Y.W.; validation, C.D., X.L., N.L. and S.L.; formal analysis, C.D., Z.Q. and S.Y.; investigation, C.D., S.Y., Y.W., N.L., S.L. and Y.L.; resources, X.L.; data curation, C.D., Z.Q. and

Y.W.; writing—original draft preparation, C.D.; writing—review and editing, X.L., Z.Q., S.Y., Y.W., N.L., S.L. and Y.L.; visualization, C.D., Z.Q. and S.Y.; supervision, X.L.; project administration, X.L.; funding acquisition, C.D. and X.L. All authors have read and agreed to the published version of the manuscript.

Funding: This article was supported by Heilongjiang Provincial Natural Science Foundation of China (Grant No. PL2025D007). This research was also supported by the Fundamental Research Funds for the Central Universities (2572017CA02), and the Harbin University Youth Doctoral Research Startup Fund (Grant No. HUDF2023107).

Institutional Review Board Statement: Not applicable.

Informed Consent Statement: Not applicable.

Data Availability Statement: Data are available upon request to the corresponding authors.

Conflicts of Interest: The authors declare no conflicts of interest.

References

1. Franklin, S.E. *Remote Sensing for Sustainable Forest Management*; CRC Press: Boca Raton, FL, USA, 2001. [CrossRef]
2. Lim, K.; Treitz, P.; Wulder, M.; St-Onge, B.; Flood, M. LiDAR remote sensing of forest structure. *Prog. Phys. Geogr.* **2003**, *27*, 88–106. [CrossRef]
3. Hyyppa, J.; Yu, X.; Hyyppa, H.; Vastaranta, M.; Holopainen, M.; Kukko, A.; Kaartinen, H.; Jaakkola, A.; Vaaja, M.; Koskinen, J.; et al. Advances in forest inventory using airborne laser scanning. *Remote Sens.* **2012**, *4*, 1190–1207. [CrossRef]
4. Mozgeris, G.; Balenovic, I. Operationalization of remote sensing solutions for sustainable forest management. *Remote Sens.* **2021**, *13*, 572. [CrossRef]
5. Zhen, Z.; Quackenbush, L.J.; Zhang, L. Trends in automatic individual tree crown detection and delineation: Evolution of LiDAR data. *Remote Sens.* **2016**, *8*, 333. [CrossRef]
6. Naveed, F.; Hu, B.; Wang, J.; Hall, G.B. Individual tree crown delineation using multispectral LiDAR data. *Sensors* **2019**, *19*, 5421. [CrossRef] [PubMed]
7. Dalponte, M.; Frizzera, L.; Gianelle, D. Individual tree crown delineation and tree species classification with hyperspectral and LiDAR data. *PeerJ* **2019**, *6*, e6227. [CrossRef] [PubMed]
8. Kempf, C.; Tian, J.; Kurz, F.; D'Angelo, P.; Reinartz, P. Oblique view individual tree crown delineation. *Int. J. Appl. Earth Obs. Geoinf.* **2021**, *99*, 102314. [CrossRef]
9. Bian, Y.; Zou, P.; Shu, Y.; Yu, R. Individual tree delineation in deciduous forest areas with LiDAR point clouds. *Can. J. Remote Sens.* **2014**, *40*, 152–163. [CrossRef]
10. Wu, B.; Yu, B.; Wu, Q.; Huang, Y.; Chen, Z.; Wu, J. Individual tree crown delineation using localized contour tree method and airborne LiDAR data in coniferous forests. *Int. J. Appl. Earth Obs. Geoinf.* **2016**, *52*, 82–94. [CrossRef]
11. Barnes, C.; Balzter, H.; Barrett, K.; Eddy, J.; Milner, S.; Suarez, J.C. Individual tree crown delineation from airborne laser scanning for diseased larch forest stands. *Remote Sens.* **2017**, *9*, 231. [CrossRef]
12. Corte, A.P.D.; da Cunha Neto, E.M.; Rex, F.E.; Souza, D.V.; Sanquetta, C.R.; Mohan, M.; Silva, C.A. High-density UAV-LiDAR in an integrated crop-livestock-forest system: Sampling forest inventory or forest inventory based on individual tree detection (ITD). *Drones* **2022**, *6*, 48. [CrossRef]
13. Corte, A.P.D.; Souza, D.V.; Rex, F.E.; Sanquetta, C.R.; Mohan, M.; Silva, C.A.; Zambrano, A.M.A.; Prata, G.A.; de Almeida, D.R.A.; Trautenmuller, J.W.; et al. Forest inventory with high-density UAV-Lidar: Machine learning approaches for predicting individual tree attributes. *Comput. Electron. Agric.* **2020**, *179*, 105815. [CrossRef]
14. Zhang, C.; Zhou, Y.; Qiu, F. Individual tree segmentation from LiDAR point clouds for urban forest inventory. *Remote Sens.* **2015**, *7*, 7892–7913. [CrossRef]
15. Rodriguez-Puerta, F.; Gomez-Garcia, E.; Martin-Garcia, S.; Perez-Rodriguez, F.; Sanchez-Sastre, L.F.; Perez-Romero, J.; Taboada, M.F. UAV-based LiDAR scanning for individual tree detection and height measurement in young forest permanent trials. *Remote Sens.* **2022**, *14*, 170. [CrossRef]
16. Mohan, M.; Leite, R.V.; Broadbent, E.N.; Wan Mohd Jaafar, W.S.; Srinivasan, S.; Bajaj, S.; Dalla Corte, A.P.; do Amaral, C.H.; Gopan, G.; Saad, S.N.M.; et al. Individual tree detection using UAV-lidar and UAV-SfM data: A tutorial for beginners. *Open Geosci.* **2021**, *13*, 1028–1039. [CrossRef]
17. Marcello, J.; Spinola, M.; Albors, L.; Marques, F.; Rodes, I.; Fita, J. Performance of individual tree segmentation algorithms in forest ecosystems using UAV LiDAR data. *Drones* **2024**, *8*, 772. [CrossRef]

18. Chen, W.; Hu, X.; Chen, W.; Hong, Y.; Yang, M. Airborne LiDAR remote sensing for individual tree forest inventory using trunk detection-aided mean shift clustering techniques. *Remote Sens.* **2018**, *10*, 1078. [CrossRef]
19. Hao, Y.; Widagdo, F.R.A.; Liu, X.; Quan, Y.; Dong, L.; Li, F. Individual tree diameter estimation in small-scale forest inventory using UAV laser scanning. *Remote Sens.* **2021**, *13*, 24. [CrossRef]
20. Lin, Y.C.; Liu, J.; Fei, S.; Habib, A. Leaf-off and leaf-on UAV LiDAR surveys for single-tree inventory in forest plantations. *Drones* **2021**, *5*, 115. [CrossRef]
21. Mielcarek, M.; Sterenczak, K.; Khosravipour, A. Testing and evaluating different LiDAR-derived canopy height model generation methods for tree height estimation. *Int. J. Appl. Earth Obs. Geoinf.* **2018**, *71*, 132–142. [CrossRef]
22. Wang, L.; Zhang, R.; Zhang, L.; Yi, T.; Chen, Y. Research on individual tree canopy segmentation of Camellia oleifera based on a UAV-LiDAR system. *Agriculture* **2024**, *14*, 364. [CrossRef]
23. Lisiewicz, M.; Kaminska, A.; Sterenczak, K. Recognition of specified errors of individual tree detection methods based on canopy height model. *Remote Sens. Appl. Soc. Environ.* **2022**, *25*, 100690. [CrossRef]
24. Zhang, Z.; Wang, J.; Li, Z.; Zhao, Y.; Yang, B. Optimization method of airborne LiDAR individual tree segmentation based on Gaussian mixture model. *Remote Sens.* **2022**, *14*, 6167. [CrossRef]
25. Chen, Q.; Gao, T.; Zhu, J.; Wu, F. Individual tree segmentation and tree height estimation using leaf-off and leaf-on UAV-LiDAR data in dense deciduous forests. *Remote Sens.* **2022**, *14*, 2787. [CrossRef]
26. Mohan, M.; Silva, C.A.; Klauberg, C.; Jat, P.; Catts, G.; Cardil, A.; Hudak, A.T.; Dia, M. Individual tree detection from unmanned aerial vehicle (UAV) derived canopy height model in an open canopy mixed conifer forest. *Forests* **2017**, *8*, 340. [CrossRef]
27. Itakura, K.; Hosoi, F. Automatic individual tree detection and canopy segmentation from three-dimensional point cloud images obtained from ground-based lidar. *J. Agric. Meteorol.* **2018**, *74*, 109–113. [CrossRef]
28. Argamosa, R.J.L.; Paringit, E.C.; Quinton, K.R.; Tandoc, F.A.M. Fully automated GIS-based individual tree crown delineation based on curvature values from a LiDAR derived canopy height model in a coniferous plantation. *Int. Arch. Photogramm. Remote Sens. Spat. Inf. Sci.* **2016**, *XLI-B8*, 563–569. [CrossRef]
29. Millikan, P.H.K.; Silva, C.A.; Rodriguez, L.C.E.; Oliveira, T.M.; Carvalho, S.P.C.; Calegario, N.; Macedo, R.L.G.; Lima, M.P.; Gorgens, E.B. Automated individual tree detection in Amazon tropical forest from airborne laser scanning data. *CERNE* **2019**, *25*, 273–282. [CrossRef]
30. Tonolli, S.; Dalponte, M.; Vescovo, L.; Rodeghiero, M.; Bruzzone, L.; Gianelle, D. Mapping and modeling forest tree volume using forest inventory and airborne laser scanning. *Eur. J. For. Res.* **2011**, *130*, 569–577. [CrossRef]
31. Cosenza, D.N.; Soares, V.P.; Leite, H.G.; Gleriani, J.M.; Amaral, C.H.; Gripp, J., Jr.; Silva, A.A.L. Airborne laser scanning applied to eucalyptus stand inventory at individual tree level. *Pesqui. Agropecu. Bras.* **2018**, *53*, 1373–1382. [CrossRef]
32. Sterenczak, K. Factors influencing individual tree crowns detection based on airborne laser scanning data. *For. Res. Pap.* **2013**, *74*, 323–333. [CrossRef]
33. Lamprecht, S.; Hill, A.; Stoffels, J.; Udelhoven, T. A machine learning method for co-registration and individual tree matching of forest inventory and airborne laser scanning data. *Remote Sens.* **2017**, *9*, 505. [CrossRef]
34. Brodic, N.; Cvijetinovic, Z.; Milenkovic, M.; Kovacevic, J. Refinement of individual tree detection results obtained from airborne laser scanning data for a mixed natural forest. *Remote Sens.* **2022**, *14*, 5345. [CrossRef]
35. Pedersen, R.O.; Bollandsas, O.M.; Gobakken, T.; Naesset, E. Deriving individual tree competition indices from airborne laser scanning. *For. Ecol. Manag.* **2012**, *280*, 150–165. [CrossRef]
36. Liu, H.; Wu, C. Tree crown width estimation using discrete airborne LiDAR data. *Can. J. Remote Sens.* **2016**, *42*, 610–618. [CrossRef]
37. Unger, D.R.; Hung, I.K.; Brooks, R.; Williams, H. Estimating number of trees, tree height and crown width using Lidar data. *GISci. Remote Sens.* **2014**, *51*, 227–238. [CrossRef]
38. Ahmad Zawawi, A.; Shiba, M.; Jemali, N.J.N. Accuracy of LiDAR-based tree height estimation and crown recognition in a subtropical evergreen broad-leaved forest in Okinawa, Japan. *For. Syst.* **2015**, *24*, e002. [CrossRef]
39. Hunter, M.O.; Keller, M.; Victoria, D.; Morton, D.C. Tree height and tropical forest biomass estimation. *Biogeosciences* **2013**, *10*, 8385–8399. [CrossRef]
40. Fu, W.; Guo, H.; Song, P.; Tian, B.; Zhang, H. Combination of PolInSAR and LiDAR techniques for forest height estimation. *IEEE Geosci. Remote Sens. Lett.* **2017**, *14*, 1218–1222. [CrossRef]
41. Li, W.; Guo, Q.; Jakubowski, M.K.; Kelly, M. A new method for segmenting individual trees from the Lidar point cloud. *Photogramm. Eng. Remote Sens.* **2012**, *78*, 75–84. [CrossRef]
42. Li, D.; Guo, H.; Wang, C.; Li, W.; Chen, J.; Zuo, Z. Individual tree delineation in windbreaks using airborne-laser-scanning data and unmanned aerial vehicle stereo images. *IEEE Geosci. Remote Sens. Lett.* **2016**, *13*, 1330–1334. [CrossRef]
43. Nemmaoui, A.; Aguilar, F.J.; Aguilar, M.A.; Sanchez-Azofeifa, G.A.; Nemmaoui, A. Benchmarking of individual tree segmentation methods in Mediterranean forest based on point clouds from unmanned aerial vehicle imagery and low-density airborne laser scanning. *Remote Sens.* **2024**, *16*, 3974. [CrossRef]

44. Shimizu, K.; Nishizono, T.; Kitahara, F.; Fukumoto, K.; Saito, H. Integrating terrestrial laser scanning and unmanned aerial vehicle photogrammetry to estimate individual tree attributes in managed coniferous forests in Japan. *Int. J. Appl. Earth Obs. Geoinf.* **2022**, *106*, 102658. [CrossRef]
45. Fankhauser, K.E.; Strigul, N.S.; Gatziolis, D. Augmentation of traditional forest inventory and airborne laser scanning with unmanned aerial systems and photogrammetry for forest monitoring. *Remote Sens.* **2018**, *10*, 1562. [CrossRef]
46. Wang, Y.; Kukko, A.; Hyyppa, E.; Hakala, T.; Yu, X.; Kaartinen, H.; Hyyppa, J. Seamless integration of above- and under-canopy unmanned aerial vehicle laser scanning for forest investigation. *For. Ecosyst.* **2021**, *8*, 9. [CrossRef]
47. Sumnall, M.J.; Albaugh, T.J.; Carter, D.R.; Cook, R.L.; Rubilar, R.A.; Montes, C.R. Effect of varied unmanned aerial vehicle laser scanning pulse density on accurately quantifying forest structure. *Int. J. Remote Sens.* **2022**, *43*, 721–750. [CrossRef]
48. Wallace, L.; Watson, C.; Lucieer, A.; Turner, D. Detecting pruning of individual stems using airborne laser scanning data captured from an unmanned aerial vehicle. *Int. J. Appl. Earth Obs. Geoinf.* **2014**, *30*, 76–85. [CrossRef]
49. Singh, K.D. Remote sensing applications in forest inventory. In *Capacity Building for the Planning, Assessment and Systematic Observations of Forests*; Springer: Berlin/Heidelberg, Germany, 2013; pp. 115–130. [CrossRef]
50. Nandasena, W.D.K.V.; Brabyn, L.; Serrao-Neumann, S. Using remote sensing for sustainable forest management in developing countries. In *The Palgrave Handbook of Global Sustainability*; Springer Nature: Cham, Switzerland, 2023; pp. 487–508. [CrossRef]
51. Nie, S.; Wang, C.; Dong, P.; Xi, X.; Wang, J.; Qin, H. A revised progressive TIN densification for filtering airborne LiDAR data. *Measurement* **2017**, *104*, 70–77. [CrossRef]
52. Zhao, X.; Guo, Q.; Su, Y.; Xue, B. Improved progressive TIN densification filtering algorithm for airborne LiDAR data in forested areas. *ISPRS J. Photogramm. Remote Sens.* **2016**, *117*, 79–91. [CrossRef]
53. Zhang, J.; Lin, X. Filtering airborne LiDAR data by embedding smoothness-constrained segmentation in progressive TIN densification. *ISPRS J. Photogramm. Remote Sens.* **2013**, *81*, 44–59. [CrossRef]
54. Cai, S.; Zhang, W.; Liang, X.; Wan, P.; Qi, J.; Yu, S.; Yan, G.; Shao, J. Filtering airborne LiDAR data through complementary cloth simulation and progressive TIN densification filters. *Remote Sens.* **2019**, *11*, 1037. [CrossRef]
55. Li, H.; Ye, C.; Guo, Z.; Wei, R.; Gao, X.; Li, J. A fast progressive TIN densification filtering algorithm for airborne LiDAR data using adjacent surface information. *IEEE J. Sel. Top. Appl. Earth Obs. Remote Sens.* **2021**, *14*, 12492–12503. [CrossRef]
56. Shi, X.; Ma, H.; Chen, Y.; Zhang, L.; Zhou, W. A parameter-free progressive TIN densification filtering algorithm for lidar point clouds. *Int. J. Remote Sens.* **2018**, *39*, 6969–6982. [CrossRef]
57. Kang, X.; Liu, J.; Lin, X. Streaming progressive TIN densification filter for airborne LiDAR point clouds using multi-core architectures. *Remote Sens.* **2014**, *6*, 7212–7232. [CrossRef]
58. Miraki, M.; Sohrabi, H.; Fatehi, P.; Kneubuehler, M. Individual tree crown delineation from high-resolution UAV images in broadleaf forest. *Ecol. Inform.* **2021**, *61*, 101207. [CrossRef]
59. Bayat, F.; Arefi, H.; Alidoost, F. Individual tree detection and determination of tree parameters using UAV-based LiDAR data. *Int. Arch. Photogramm. Remote Sens. Spat. Inf. Sci.* **2019**, *XLII-4/W18*, 179–182. [CrossRef]
60. Zaforemska, A.; Xiao, W.; Gaulton, R. Individual tree detection from UAV LiDAR data in a mixed species woodland. *Int. Arch. Photogramm. Remote Sens. Spat. Inf. Sci.* **2019**, *XLII-2/W13*, 657–663. [CrossRef]